Check for updates

Encapsulation of Ti$_x$Fe$_y$La$_m$O$_z$ nanoparticles into NH$_2$-MIL-125(Ti) to fabricate a promising photocatalyst for the C–N coupling reaction†

Yahya Absalan, [iD] *[a] Mohammad Rafsanjani Dehghazi, [iD] [b] Reza Samavati,[c] Kambiz Souri[d] and Mostafa Gholizadeh [iD] [b]

An array of organic compounds and natural products can be synthesized through carbon–nitrogen coupling reactions. Photocatalysts are used with different structures, considering their advantages such as purity, low cost, and use of sunlight as an energy source. Metal–organic frameworks (MOFs), with their high surface activity, facile electron migrations, and stability, are highlighted. In this study, we synthesized a new composite by encapsulating Ti$_x$Fe$_y$La$_m$O$_z$ nanoparticles at different concentrations into NH$_2$-MIL125(Ti). Several types of analyses were used to characterize the obtained composites and measure their optical properties, including X-ray diffraction, high-resolution transmission electron microscopy, energy-dispersive X-ray spectroscopy, field emission scanning electron microscopy, Fourier transform infrared spectroscopy, diffuse reflectance UV/vis spectra, photoluminescence, nuclear magnetic resonance spectroscopy, mass spectrometry, Brunauer–Emmett–Teller surface area measurement, cyclic voltammetry, inductively coupled plasma, and photocurrent spectroscopy. The obtained composite was used as a photocatalyst for the carbon–nitrogen coupling reactions of aniline and ten different derivatives. La(1.05)@MOF (second lowest concentration) showed the highest photocatalytic activity under visible light to power the C–N coupling reaction. In addition, we performed an in-depth study on the mechanism of these composites and the pathway of electron migration, which have rarely been reported. We found that the optimum loading concentration can assist in increasing the optical and physical properties of photocatalysts, which consequently leads to significant improvement in the C–N coupling reactions to obtain an 80% yield.

[a] *Department of Chemistry, University of Georgia, Athens, Georgia 30602, USA. E-mail: Yahya.absalan@uga.edu; Tel: +1 (706) 2079689*

[b] *Department of Chemistry, Faculty of Science, Ferdowsi University of Mashhad, Mashhad, Islamic Republic of Iran*

[c] *Department of Organic Chemistry, RUDN University, 6 Miklukho-Maklaya St., Moscow 117198, Russia*

[d] *Department of Mechanical and Instrumental Engineering, Academy of Engineering, RUDN University, 6 Miklukho-Maklaya Street, Moscow 117198, Russia*

† Electronic supplementary information (ESI) available: The color of the different samples (Fig. S1), photocatalytic C–N cross-coupling reaction (Fig. S2), PXRD pattern of (a) Ti$_x$Fe$_y$O$_z$, and (b) Ti$_x$Fe$_y$La$_m$O$_z$ (Fig. S3), PXRD pattern of (a) pristine MOF, (b) La@MOF, and (c) Fe@MOF (Fig. S4), FT-IR spectroscopy of Fe@MOF (Fig. S5), FESEM image of (a) Ti$_x$Fe$_y$O$_z$, (b) Fe@MOF (Fig. S6), EDX analysis of La(1)@MOF (Fig. S7), EDX analysis of La(1.1)@MOF (Fig. S8), EDX analysis of La(1.15)@MOF (Fig. S9), photocurrent transient response of Ti$_x$Fe$_y$O$_z$, and Ti$_x$Fe$_y$La$_m$O$_z$ nanoparticles under visible light irradiation (Fig. S10), (a) diffuse reflectance spectra of the Ti$_x$Fe$_y$O$_z$ and Ti$_x$Fe$_y$La$_m$O$_z$ nanoparticles; (b) UV-vis spectra of the Ti$_x$Fe$_y$O$_z$ and Ti$_x$Fe$_y$La$_m$O$_z$ nanoparticles; (c) the energy bandgap of the Ti$_x$Fe$_y$O$_z$ and Ti$_x$Fe$_y$La$_m$O$_z$ nanoparticles under the indirect transition assumption (Fig. S11), (a) CV analysis of the Ti$_x$Fe$_y$O$_z$ nanoparticles and the (b) Ti$_x$Fe$_y$La$_m$O$_z$ nanoparticles (Fig. S12), producer for the synthesis of all of the derivatives; ^{1}H-NMR spectra, FT-IR spectroscopy, and mass spectrometry of derivative reactions (Fig. S13–S48), the data for La@MOF with different loadings of the Ti$_x$Fe$_y$La$_m$O$_z$ nanoparticle (Table S1), chemicophysical features of the samples (Table S2). See DOI: https://doi.org/10.1039/d3re00457k

1. Introduction

Due to its low cost and proficiency in synthesizing new compounds such as drug candidates and agricultural compounds, C–N cross-coupling is a momentous transformation in organic chemistry.[1–3] Although there have been many considerable advancements of this reaction, it is very important to use methods to remove or reduce some of the required components of the reaction such as temperature, and carry out this reaction in a greener environment, *e.g.*, using green solvent. Applying those photocatalysts that do not require the use of ligand would also be of great assistance. Among the various treatments, there has been considerable research on semiconductor photocatalysts that have the ability to perform reactions under visible light.[4–10]

TiO$_2$ has been frequently investigated, and it has become the most promising photocatalyst to use in organic reactions due to its high efficiency, high photocatalytic activity, nanotoxicity, cost-effectiveness, and chemical stability.[11–15] Nevertheless, because of the wide band gap of pristine titanium dioxide (TiO$_2$), it is inefficient for carrying out reactions under visible light.[16] To produce a photocatalyst

This journal is © The Royal Society of Chemistry 2024

React. Chem. Eng., 2024, 9, 849–860 | 849

with the ability to operate under visible light, different methods exist, among which doping TiO_2 with metals can transfer the active area of TiO_2 from ultraviolet light to visible light. It is even possible to increase the active surface of modified TiO_2 using lanthanides,[17] which can be performed by a co-doping method, and this consequently increases the photocatalytic reactivity.[18–20]

Metal–organic frameworks (MOFs),[21] due to their large internal surface area,[22] flexibility in designing the active sites,[23] chemical alteration,[24] pore structure, and high metal content,[25] provide valuable opportunities to design compounds with multiple applications.[26] MOFs are less thermally and chemically stable compared to porous mineral solids, even though some of them decompose when exposed to air or moisture.[27] Considering the high surface area and porous structure of MOFs,[28] it is possible to introduce photosensitizers such as polyoxometalates (POMs),[29] metal/metal oxide nanoparticles, or semiconductors[30] that increase the photocatalytic efficiency and confer greater stability under moist conditions.[31] For this purpose, some strategies have been conducted that incorporate specific catalytic activity into MOFs, *e.g.*, sites on metal species, organic linkers (ligands such as benzene dicarboxylate), post-synthetic modification grafted sites,[32] catalytically active sites,[33] and encapsulated MOF composition sites.[34,35] Using the functionalized cavities of MOFs as active sites for metal nanoparticles seems promising for the development of high-performance heterogeneous catalysts.[36]

Recently, new properties have led to an increase in the encapsulation of nanoparticle MOFs[37] as a result of the synergistic effect between two functional materials,[38–40] and they tend to show higher activity and increased selectivity compared to their pristine counterparts. The encapsulation of noble-free nanoparticles in a MOF is a relatively new branch in the MOF family, and can be performed for those MOFs that exhibit excellent shape and selective catalytic performance in organic reactions.[38,41]

To achieve this, NH_2-MIL-125(Ti) was chosen to be modified by a tri-nuclear nanoparticle of $Ti_xFe_yLa_mO_z$, which we recently obtained in our group[17] and used in a photocatalytic C–N cross-coupling reaction under visible light, with $Ti_xFe_yLa_m$-O_z@NH_2-MIL-125 prepared by the impregnation method. The obtained composite illustrated the ability to successfully synthesize the product in a short time without using any basis, with a high product yield and stability over several cycles.

2. Experimental

2.1. Materials and reagents

All the materials and precursors, including titanium, lanthanum, iron salts, 2-aminoterephthalic acid, and solvents, were high-purity chemicals obtained from Sigma-Aldrich, and they were used without further purification.

2.2. Syntheses

Synthesis of $Ti_xFe_yO_z$ and $Ti_xFe_yLa_mO_z$ nanoparticles. The synthesis of nanoparticles was conducted as follows. Initially, one mole of titanium butoxide, serving as a titanium precursor, was dissolved in 25 milliliters of deionized water (solution A). Subsequently, 0.5 moles of iron chloride salt, functioning as an iron precursor, was dissolved in an equal volume of deionized water (solution B). Solutions A and B were combined and stirred for 15 minutes using a magnetic stirrer. Afterwards, an ammonia solution (24 mL of ammonia and 15 mL of deionized water) was added dropwise, and the mixture was stirred for 24 hours. Iron-doped titanium oxide nanoparticles were ultimately acquired through a hydrothermal process employing an autoclave for 24 hours at 113 °C (the temperature range tested was 100 °C to 150 °C). Separation and purification involved centrifuging the resulting solution twice to eliminate the solvent, followed by the use of deionized water for purification. The product was placed at 80 °C for 24 hours to completely dry, and was subsequently calcined at 450 °C at a rate of 10 °C per minute.

The same procedure was employed for the synthesis of double-doped nanoparticles with transition metals and lanthanum, with the exception that the lanthanum solution (0.5 moles in 25 mL of deionized water) was introduced as solution C to solutions A and B.

Synthesis of the pristine MOF. Pristine MOF synthesis involved the addition of 10 mmol of titanium butoxide to 40 mL of solvent, comprising a methanol and DMF mixture at a 9 : 1 ratio (9 parts methanol), and subjecting it to ultrasonic treatment at 180 W for 2 h. Subsequently, 15.8 mL of 2-amino terephthalic acid was added, and the mixture was stirred for 154 minutes utilizing a magnetic stirrer. The solution was transferred to an autoclave and maintained at 110 °C for 72 hours. The autoclave was then cooled to room temperature, and its contents were separated using a centrifuge. The contents were washed twice with DMF and twice with methanol, with the remaining residues were transferred to a vacuum oven and heated at 50 °C for 24 hours.

To obtain MOFs with high crystallinity, the obtained MOF was poured into 100 ml boiling DMF under reflux for 5 hours. Then, it was centrifuged and dried under a vacuum at 50 °C.

Encapsulation of the nanoparticles in MOFs. For encapsulated MOF synthesis, an encapsulation method was employed. First, 10 mmol of titanium butoxide and 10 μmol of nanoparticles were simultaneously placed in 40 mL of solvent (methanol and DMF mixture at a 9 : 1 ratio), which was subjected to ultrasonic treatment at 180 W for 2 h. Thereafter, 15.8 mL of 2-amino terephthalic acid was added to the solution, which was then vigorously stirred for 15 minutes using a magnetic stirrer. The solution was transferred to an autoclave and maintained at 110 °C for 72 h. After completing this period, the autoclave was cooled to room temperature, and its contents were washed twice with methanol and twice with DMF to remove unreacted reactants and solvents remaining in the pores. The residues were transferred to a vacuum oven and heated for 24 h at 50 °C, and the dried residues were subsequently ground using a mortar. The mentioned amount refers to the 10% concentration of the nanoparticle. Table S1† shows other concentrations, and the color of the obtained compounds can be seen in Fig. S1.†

Photocatalytic C–N cross-coupling reaction. To determine the most optimal conditions, aniline (0.25 mmol, 0.02 g) was added to different solvents (2 mL), and the mixture was stirred. After a few minutes, 1-chloro-2,4-dinitrobenzene (0.35 mmol, 0.07 g) and catalyst (0.01 g) were added. The reaction mixture was examined under different conditions (Table 3), and the reaction was also monitored by thin-layer chromatography (TLC). The catalyst was separated after the completion of the reaction. The desired product was extracted with ethyl acetate (4 mL), and the obtained crude product was purified by ethyl acetate. TLC using n-hexane/ethyl acetate (5:2) solvent was also used to detect the product (Fig. S2†).

2.3. Characterization and methods

X-ray diffraction (XRD) was carried out using a GNR Explorer advance with 1.541 A (Cu-Ka). The corresponding degree for the experiment was between 5° and 40° for the MOFs and 10° to 90° for the nanoparticles. High-resolution transmission electron microscopy (HRTEM) was performed using an FEI Tecnai TF20 electron microscope with a field emission gun as the source of electrons operated at 200 kV. Energy-dispersive X-ray spectroscopy (EDX) was carried out using an LEO 912AB TEM instrument. Field emission scanning electron microscopy (FESEM) was performed using a TESCAN BRNO-Mira3 LMU. Fourier transform infrared (FT-IR) spectroscopy was recorded on pressed KBr pellets using an AVATAR 370 FT-IR spectrometer (Thermo Nicolet, USA) at room temperature in the range of 4000–400 cm^{-1} at a resolution of 4 cm^{-1}. Diffuse reflectance UV/vis spectroscopy (DRS) was performed, and spectra were obtained using an Avantes Avaspec-2048-TEC in the range between 200 and 800 nm. The standard used for the analysis was $BaSO_4$. UV/vis spectroscopy was performed using a Cary-50 scanning spectrophotometer (Varian) device at room temperature, with ethanol as the solvent. A Tauc plot was used to obtain the energy bandgap of the composites through the $\alpha = \alpha_0(h\nu - E_g)^n/h\nu$ formula, where α denotes the absorption coefficient, $h\nu$ denotes the photon energy α_0, h denotes Planck's constant, E_g denotes the optical band gap of the material, and the value of n is between 0.5 and 3, depending on the character of the electronic transition. Photoluminescence (PL) detection was achieved using the Avantes-Avaspec-2048. Photoluminescence emission spectra of the samples were recorded upon excitation at 355 nm based on the UV-vis spectroscopy results. Nuclear magnetic resonance (NMR) spectroscopy was performed using an NMR Bruker Avance spectrometer, at 300 and 400 MHz in DMSO. Mass spectrometry (MS) was performed with a CH7A Varianmat Bremem instrument at 70 eV electron impact ionization, in m/z (rel%).

To determine the surface activity of the samples, the Brunauer–Emmett–Teller (BET) surface area was measured using capillary condensation of nitrogen at 77 K on a micrometric Belsorp-Mini II (Microtrac) system analyzer.

Prior to the measurements, the samples were degassed at 423 K under a vacuum for 5 hours. The BET surface areas were calculated using intervals allowing positive BET constants. The total pore volumes were calculated at 0.9 relative pressure. Cyclic voltammetry (CV) was carried out using the usual three-electrode system, including the working electrode (glassy carbon electrode (d = 2 mm)), reference electrode (Ag/AgCl saturated by KCl), and counter electrode (platinum wire). N_2 was used for saturating the experimental environment, and it was purged 15 minutes before the experiment. The potential window was set between −2.5 and 0 V with a scan rate of 50 mV s^{-1}. An IUPAC system was used for the analysis, and thus, the flow motion was from the right to the left. An electrolyte of 0.1 mol of $[(nBu)_4N]$ $[PF_6]$ in 10 mL CH_3CN was used. Inductively coupled plasma-optic emission spectroscopy (ICP-OES) was performed using a 76004555-Spectro Arcos spectrometer. The sample was dissolved in a mixture of nitric acid, hydrochloric acid, and hydrogen peroxide and placed at 80 °C for 2 hours. Then, it was diluted with deionized water to a volume of 100 ml, and finally, it was filtered and used for analysis. Photocurrent spectroscopy (PCS) was achieved with a xenon 100 W lamp at a potential of 0.0 V.

3. Results and discussion

3.1. Material characterization

Powder X-ray diffraction (PXRD) analysis. The PXRD analysis was used to determine the crystallite structure of the existing nanoparticles, MOFs, and modified MOFs (Fig. 1). Two samples of $Ti_xFe_yO_z$ and $Ti_xFe_yLa_mO_z$ nanoparticles, which were previously obtained, were used for this work (Fig. S3†).[17] The overall crystallite structure for both samples showed the anatase phase, which is one of the phases of TiO_2. However, in each case, the peak related to the corresponding elements can be observed and is illustrated in the figure (Fig. S3a and b†). The details related to each sample are shown in Table S2.† The increase in the size is
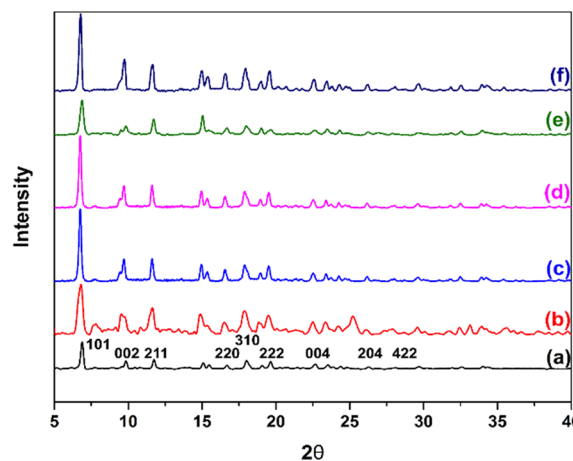

Fig. 1 PXRD pattern of (a) pristine MOF, (b) Fe@MOF (c) La(1)@MOF and (d) La(1.05)@MOF (e) La(1.1)@MOF and (f) La(1.15)@MOF.

related to the number of nuclei in the final compounds that attract the outer electrons, which was observed for Fe and La elements.

The PXRD of the pristine MOF, Fe@MOF, and La@MOF is illustrated in Fig. S4.† Crystallite MOF was obtained, with the corresponding peaks related to the MOF (Fig. S4a†). After encapsulation of $Ti_xFe_yO_z$ and $Ti_xFe_yLa_mO_z$, the overall structure of the pristine MOF remained with no change, and the dominant Bragg reflection was assigned to 101, which was the same as that for pristine MOF.

Fig. 1 shows a comparison of the pristine MOF and La@MOF at different concentrations. According to the results, the overall structure of the pristine MOF was unchanged, and in all the cases, the main crystallite structure was related to the pristine MOF.

FT-IR analysis. Fig. 2 illustrates the FT-IR spectroscopy of pristine MOF and La@MOF at different concentrations. Based on the results, the overall peaks in both parts of the fingerprint and group frequency were assigned to the pristine MOF. However, the encapsulation of $Ti_xFe_yLa_mO_z$ was confirmed by a change in NH_2 (symmetric NH_2 = 3455 cm^{-1}; asymmetric NH_2 = 3346 cm^{-1}), when pristine MOF was encapsulated by $Ti_xFe_yLa_mO_z$ at different concentrations, and enhancement occurred in the alkyl region. Fig. S5† shows the encapsulation of the pristine MOF by $Ti_xFe_yO_z$, and the same changes can be seen in this sample as well.

Microscopic analyses (FESEM, TEM, and HRTEM) and EDX analysis. Morphology of the different samples, including pristine MOF and La@MOFs at different concentrations (Fig. 3), modified MOF with Fe, and pure nanoparticles (Fig. S6†) illustrates that all the samples were obtained with a uniform shape and structure. Due to the different conditions (temperature and time) required to obtain the crystallite structure, the MOF has become a cubic shape (Fig. 3a). Nanoparticles of $Ti_xFe_yLa_mO_z$ and $Ti_xFe_yO_z$ were acquired with an irregular shape and a dense structure, but no accumulation was observed (Fig. 3b and S6†). After encapsulation of different nanoparticles, including $Ti_xFe_yO_z$ and $Ti_xFe_yLa_mO_z$, the structures of the modified MOFs were not changed, and the cubic shape was visible in all the
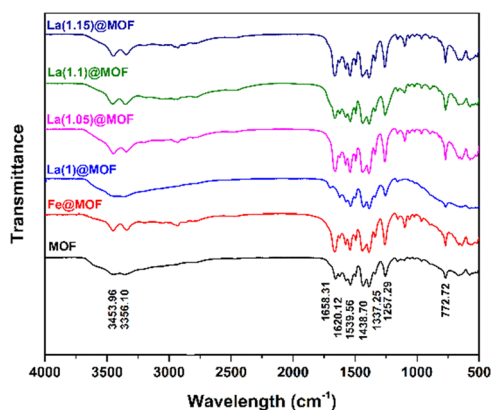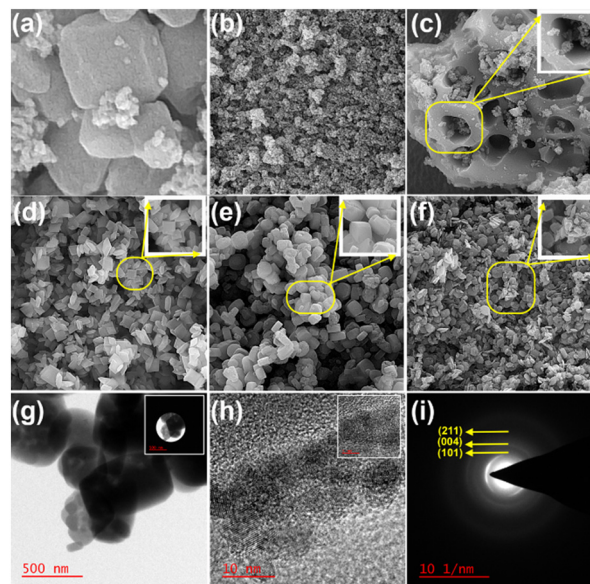

Fig. 3 FESEM image of (a) pristine MOF, (b) $Ti_xFe_yLa_mO_z$, (c) La(1) @MOF, (d) La(1.05)@MOF, (e) La(1.1)@MOF, (f) La(1.15)@MOF, (g and h) HRTEM image of La(1.05)@MOF, and (i) SAED figure of La(1.05)@MOF.

samples (Fig. 3c–e). However, in the case of La(1.15)@MOF, the cubic shape of the MOF was deformed, and it is difficult to find a regular shape, which showed that the excess amount of nanoparticles affected the morphology of the pristine MOF (Fig. 3f).

The HRTEM analysis was carried out for La(1.05)@MOF (Fig. 3g–i). Fig. 3g shows the cubic shape of La(1.05)@MOF, and it supports the shape of the pristine MOF, which is illustrated by the FESEM analysis. In addition, the bright contrast in the figure confirmed the loading of lanthanum nanoparticles. The orientation of the lanthanum crystals is illustrated in Fig. 3h. The crystallite structure of the pristine MOF after the loading of lanthanum nanoparticles was confirmed by the SAED image (Fig. 3i). The Bragg reflection of the different circle layers illustrated the Miller index obtained by the PXRD analysis (Fig. 1).

EDX mapping was performed to determine the amount of the different elements in the final composition, and the results are shown in Table 1 and Fig. 4 and S7–S9.† The results established that the corresponding elements exist with high purity in all the samples. Based on the results, the highest amount of Fe among the samples was measured for

Fig. 2 The FT-IR spectroscopy of the obtained samples.

Table 1 The elemental composition of the samples obtained by EDX

Element	La(1)@MOF	La(1.05)@MOF	La(1.1)@MOF	La(1.15)@MOF
C	33.77	50.53	47.40	54.58
N	19.64	15.81	17.18	15.09
O	36.05	24.22	27.60	24.43
Ti	10.15	9.21	7.67	5.70
Fe	0.17	0.18	0.12	0.16
La	0.23	0.04	0.03	0.04
Total	100.00	100.00	100.00	100.00

852 | *React. Chem. Eng.*, 2024, **9**, 849–860

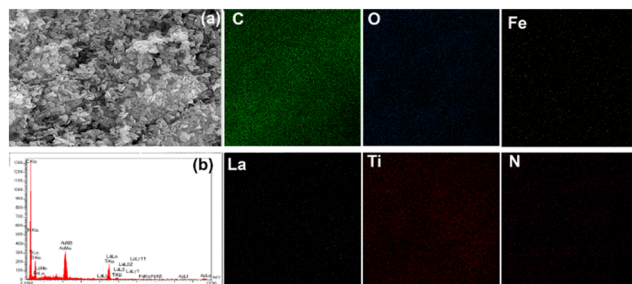This journal is © The Royal Society of Chemistry 2024

Fig. 4 FESM image of (a) La(1.05)@MOF, (b) EDX of La(1.05)@MOF, and the elemental mapping of La(1.05)@MOF.

La(1.05)@MOF, and the amount of Ti was the highest after La(1)@MOF (Fig. 4).

3.2. Catalytic characterization

BET analysis. The surface activity of the pristine MOF, La@MOF, and Fe@MOF was determined, and the results are shown in Fig. 5 and Table 2. The pristine MOF, Fe@MOF, and La@MOF illustrated the same behavior based on their types, which are matched with IV, and it shows that there is a strong relationship between the surface of the compounds and adsorption, and the compounds possess a mesopore type porosity (Fig. 5a).

The surface activity was decreased, which proved that encapsulation of the nanoparticles and blocking of some parts of the surface occurred. However, the overall surface activity remained unchanged, which showed that distortion did not occur. The Barrett–Joyner–Halenda (BJH) model was analyzed to measure the total pore volume and mean pore
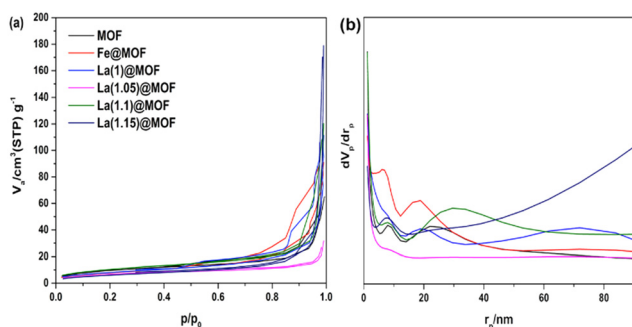
diameter (Fig. 5b). The results demonstrated that after encapsulation, the total pore volume changed and remarkably decreased compared to the pristine MOF (Table 2). Among the different composites, La(1.05)@MOF showed the highest reduction in surface activity, total pore volume, and mean pore diameter, which indicates that the highest volume of nanoparticles was encapsulated by this concentration, and it was also determined by EDX analysis.

Spectroscopy analyses. The photoluminescence results indicate that the emission of Fe@MOF and La@MOF at different concentrations is higher than that of the pristine MOF (Fig. 6a). The speed reduction of the electron recombination from LUMO to the HOMO was established due to the lower emission of the modified MOFs, which is a vital parameter for a photocatalyst because in most of the photocatalysts, the excited electrons come back to the valence band (nanoparticles) or HOMO (bulk material), and the reaction completes. According to the mentioned rule, all the modified MOFs underwent faster recombination compared to the pristine MOF, except for La(1.05)@MOF, which showed the same recombination speed. La(1.05)@MOF and La(1.15)@MOF are the only modified MOFs that were able to absorb visible light with higher intensity due to the redshift.

The photocurrent spectroscopy of the pristine MOF and La@MOFs was performed with a variety of on/off cycles (Fig. 6b). All the samples immediately responded to light after turning the light on, and came back to zero after turning the light off. Compared to the pristine MOF, all the samples illustrated a remarkable enhancement when responding to light. This shows that releasing efficient electrons occurred after the modification of the MOF by the $Ti_xFe_yLa_mO_z$ nanoparticle.

Based on the result, the electrons are more able to emigrate from the valence (highest occupied molecular orbital, HOMO) to the conduction band (lowest unoccupied molecular orbital, LUMO), and it provides more optimal conditions for the photocatalytic reaction. According to the result, the photocurrent density decreased after increasing the concentration of $Ti_xFe_yLa_mO_z$ by a small amount, which shows that there is a limitation in encapsulating $Ti_xFe_yLa_mO_z$ into the cage of the pristine MOF, and adjustment by an efficient amount was required, with the optimum by La(1.05)@MOF due to its highest photocurrent density. The photocurrent spectroscopy of the nanoparticles showed that there was a more optimal response to light by the $Ti_xFe_yLa_mO_z$ nanoparticle as compared to the $Ti_xFe_yO_z$ nanoparticle (Fig. S10†).

Fig. 5 (a) Nitrogen isotherms were recorded at 77 K. (b) Total pore volumes were calculated at 0.9 P/P_0.

Table 2 Physicochemical properties of the samples

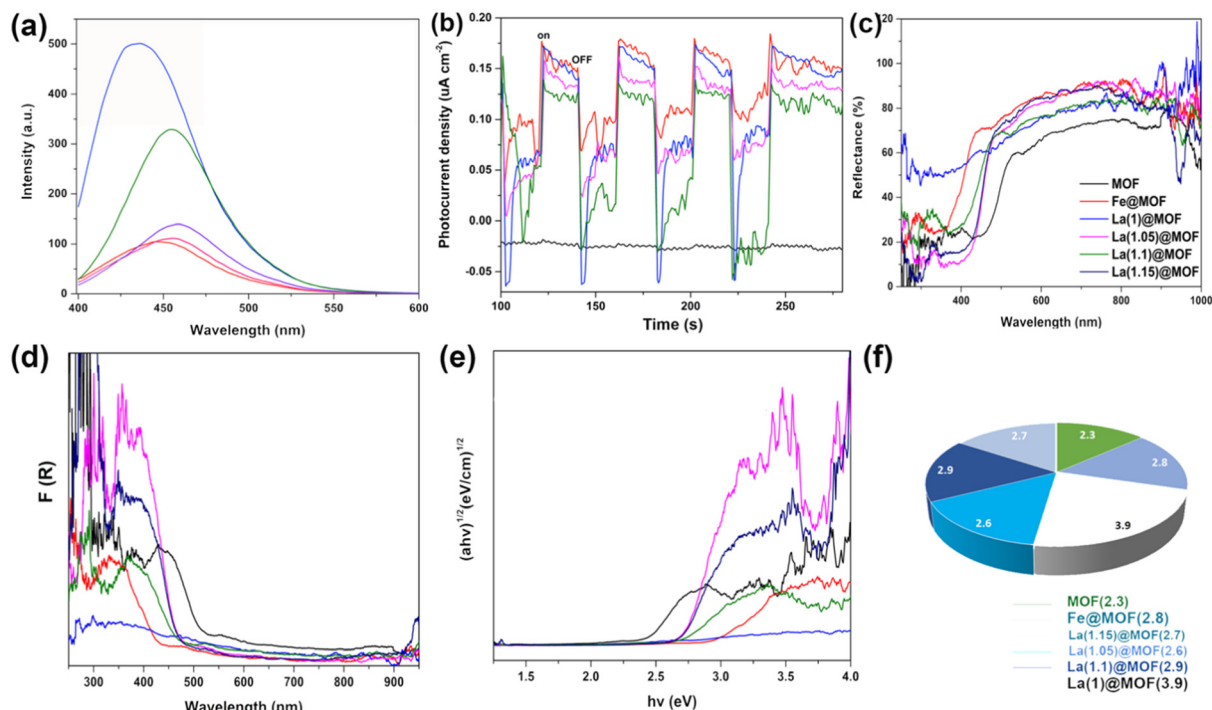| Sample	a_{BET} (m² g⁻¹)	Total pore volume (p/p_0 = 0.990) (cm³ g⁻¹)	Mean pore diameter (nm)
MOF	350.606	0.314814	51.651
Fe@MOF	290.019	0.1405	19.367
La(1)@MOF	290.575	0.1674	22.635
La(1.05)@MOF	250.162	0.047682	7.58
La(1.1)@MOF	340.938	0.1849	21.172
La(1.15)@MOF	270.043	0.2744	47.64

Fig. 6 (a) Photoluminescence emission spectra (λ_{ex} = 380 nm, refers to its UV-vis spectrum). (b) Photocurrent transient response under visible light irradiation. (c) Diffuse reflectance spectra of the composites. (d) UV-vis spectra of the composites. (e and f) The energy bandgap of the composites under the indirect transition assumption.

We converted the DRS data to the UV-vis data to acquire additional information regarding the absorption, and the $-1/(\log(1/R))$ formula was used, where R denotes the reflectance. Based on the result obtained by DRS and UV-vis spectroscopy, the wavelength and intensity were changed after encapsulation of the $Ti_xFe_yLa_mO_z$ nanoparticles (Fig. 6c and d). There is a blueshift in all the samples modified by the $Ti_xFe_yLa_mO_z$ nanoparticle. The intensities of La(1.05)@MOF and La(1.15)@MOF were higher than that of the pristine MOF, but there was nearly equal or lower intensity for the others. According to the Tauc plot analysis, the energy bandgap of the $Ti_xFe_yLa_mO_z$ nanoparticle was 2.3 eV (Fig. S11†), which is equal to the energy band gap of the pristine MOF (2.3 eV), and therefore, it could not efficiently affect the energy bandgap (Fig. 6e). According to EDX, the highest amount of Fe was contained in La(1.05)@MOF (Table 1), and this affected the obtaining of the lowest energy bandgap, and it confirmed that Fe entered the crystallite structure of Ti due to its shorter ionic radius (Ti : Fe = 176 : 156 pm, respectively).

CV analysis. Cyclic voltammetry was applied to find the place of the LUMO, and DRS analysis provided the energy bandgap of the compounds. The combination of the result extracted from the DRS and CV provided sufficient information to find the place of the HOMO (E = LUMO–HOMO). We used this method to obtain additional data regarding the electron emigration route in the obtained composite, which will be further explained in detail in the next sections. The CV analysis of $Ti_xFe_yLa_mO_z$ from the

previous work showed that the LUMO (or CB = conduction band) is located at φ_{LUMO} = −1.1 V *vs.* the vacuum (Fig. S12†). This amount was obtained through the equations of E_{CB} = −(E_{red} + 4.8) and φ_{LUMO} = −[E_{CB} − (−4.4)], which is a transformation from the potential of the catalyst to the level *vs.* vacuum. In the mentioned equation, 4.8 is the correction related to the Ag/AgCl couple and the normal hydrogen electrode (NHE). Because the reduction peak of LUMO of La(1.05)@MOF is located at E_{red}= −0.4, the E_{CB} will be equal to −4.4 eV *vs.* vacuum (Fig. 7).
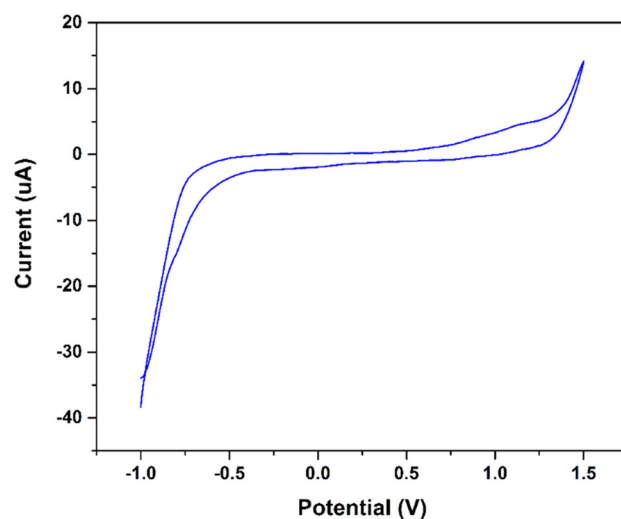

Fig. 7 CV analysis of La(1.05)@MOF.

854 | *React. Chem. Eng.*, 2024, **9**, 849–860

This journal is © The Royal Society of Chemistry 2024

Reaction Chemistry & Engineering   **Paper**

Table 3 The result obtained from different conditions

No.	Catalyst	Solvent	Time (h)	Product	Yield (%)	Light
1	MOF(0.01 g)	DMSO	24	NR	0	VIS
2	MOF(0.01 g)	CH_2Cl_2	24	NR	0	VIS
3	MOF(0.01 g)	H_2O	24	NR	0	VIS
4	MOF(0.01 g)	ETOH	24	NR	0	VIS
5	MOF(0.01 g)	Toluene	24	NR	0	VIS
6	MOF(0.01 g)	Acetonitrile	10	NC	10	VIS
7	MOF(0.01 g)	H_2O/ETOH	1	C	80	VIS
8	MOF(0.01 g)	H_2O/ETOH	1	NR	0	VIS
9	MOF(0.01 g)	H_2O/ETOH	1	NR	0	DARK
10	NO	H_2O/ETOH	1	NR	0	DARK
11	MOF(0.02 g)	H_2O/ETOH	1	C	85	VIS

NR: No reaction; C: complete.

3.3. Photocatalytic performance

The photocatalytic process was carried out with La(1.05) @MOF under different conditions to determine the most optimal situation for the synthesis of phenylaniline and its derivatives (Table 3).

The results from different conditions confirmed that the most optimal condition for the photocatalytic coupling reaction is when 0.02 g of La(1.05)@MOF were used as the catalyst at room temperature for 1 h in H_2O/ETOH solvent with a 1/1 ratio under visible light. Therefore, this condition was applied to different phenylaniline derivatives (Table 4). CNMR, mass, and FT-IR analyses related to each compound obtained from the reaction can be found in Fig. S13–S48.†

3.4. Stability test

To test the stability of La(1.05)@MOF, the most optimal rate of the carbon–nitrogen cross-coupling reaction variables was used (Fig. 8). The reaction was exposed to visible light, and after one hour in the case of the MOF, the reaction was completed, and the catalyst separation process was completed.

In the case of MOFs, to solidify the product and the catalyst, the sediments were first washed in ethyl acetate (because the product easily dissolves in this solvent) to separate the desired product and the remaining sediments containing the desired catalyst. It was washed three to four times with methanol, and the remaining solids were poured into a Falcon centrifuge tube and approximately 10 ml of methanol was added to it. After centrifugation, its impurities were absorbed by methanol in such a manner that after centrifuging twice, the methanol used did not change color, which indicates the disappearance of existing impurities.

Finally, the catalyst was placed inside a vacuum oven at a temperature of 50 °C for 24 hours. The reaction was carried out by the MOF in 7 consecutive steps, and the degree of stability was investigated by the XRD test.

3.5. Role of solvent

Different solvents used for the C–N coupling of phenylaniline (Table 3), such as polar protic solvents, are more efficient. Protic solvents can rapidly exchange due to hydrogen bonds. Otherwise, polar solvents, which possess high dielectric constants, have an effect on the reaction rates.

Reactions that involve charge separation in the transition structure (TS) rapidly proceed in protic solvent. Because of the high dielectric constants, there is significant ability by water (78) and ethanol (24.5) to respond to a change in charge distribution as the reaction occurs, and increase with molecular dipole moment and polarizability because of the ability of the permanent and induced molecular dipole to align with the external field (Fig. 9).

The ability of solvent to stabilize the TS has been measured by comparing the rate of the reaction in the different solvent mixtures according to the equation below:

$$Y = \log K_{50\%H_2O}/K_{50\%ETOH}$$

where Y represents the ability of solvent to stabilize TS, and for H_2O/ETOH (50 : 50), this number is 1.65.

Effect of solvent on the catalyst. The position of absorption bands is sensitive to solvent polarity because of the electronic distribution, and therefore, the polarity of the excited state is different from that of the ground state. The shift in the absorption maxima reflects the effect of solvent on the energy gap between the ground state and excited state molecules. An empirical solvent polarity measure called E_T (30) is based on this concept, the value of which is 63.1 for water and 51.9 for ethanol.

4. Proposed mechanism

Pathway of electrons in the photocatalyst

Based on the results obtained from the DRS and CV analyses, the pathway of electrons is shown in Fig. 10. The location of the energy bandgap of $Ti_xFe_yLa_mO_z$ and the pristine MOF is observable in Fig. 10a. In this case, the energy bandgap of pristine MOF is equal to 2.3 eV, and the HOMO and LUMO are in 2.25 eV and −0.05 eV, respectively. The energy bandgap of $Ti_xFe_yLa_mO_z$, as obtained by DRS, is equal to 2.3 eV (the same as that of pristine MOF), and its valence and conduction bands are located at 1.2 eV and −1.1 eV,

Table 4 The result obtained for the synthesis of different derivatives of aniline by La(1.05)@MOF
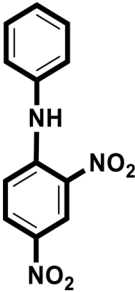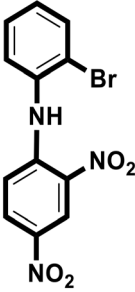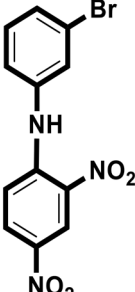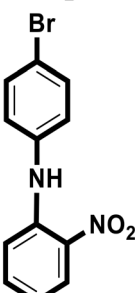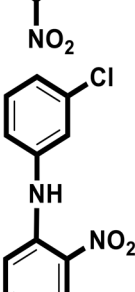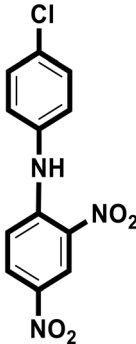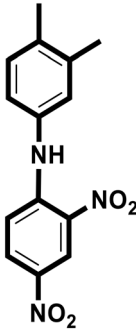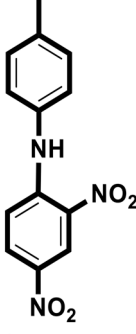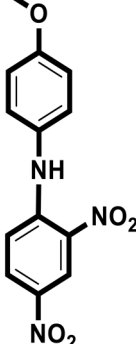
Entry	Aniline derivatives	Aniline derivatives	Product	Time (min)	Yield (%)
1	Aniline	2,4-Dinitrochlorobenzene		60	80%
2	2-Bromoaniline	2,4-Dinitrochlorobenzene		90	15%
3	3-Bromoaniline	2,4-Dinitrochlorobenzene		85	30%
4	4-Bromoaniline	2,4-Dinitrochlorobenzene		75	45%
5	3-Chloroaniline	2,4-Dinitrochlorobenzene		85	38%

856 | *React. Chem. Eng.*, 2024, **9**, 849–860

This journal is © The Royal Society of Chemistry 2024

Table 4 *(continued)*

Entry	Aniline derivatives	Aniline derivatives	Product	Time (min)	Yield (%)
6	4-Chloroaniline	2,4-Dinitrochlorobenzene		70	48%
7	3,4-Dimethylaniline	2,4-Dinitrochlorobenzene		60	62%
8	4-Methylaniline	2,4-Dinitrochlorobenzene		55	71%
9	4-Methoxyaniline	2,4-Dinitrochlorobenzene		58	69%

respectively. Based on this information, we deduced that the pristine MOF works as an antenna because its HOMO is shorter, and it absorbs light. After absorbing light by the pristine MOF and exciting electrons from the HOMO level, there are two possibilities for the migration of electrons, which are shown as pathways 1 and 2 (Fig. 10a). Pathway 1 is more possible according to exciting electrons from shorter distances. However, we cannot ignore the possibility of

pathway 3. Then, the electrons excited to the highest level (conduction band of $Ti_xFe_yLa_mO_z$: −1.1 eV) react with aniline.

Pathway of electrons in the organic reaction

Nucleophilic aromatic substitution results in the substitution of a halogen X on a benzene ring by a nucleophile. Aryl halides with strong electron-withdrawing groups (EWGs)
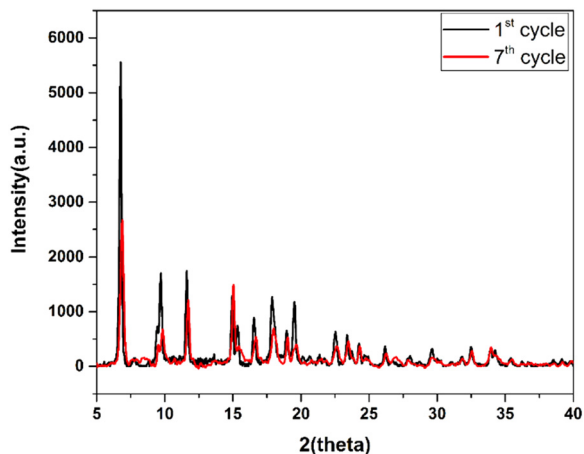
This journal is © The Royal Society of Chemistry 2024

React. Chem. Eng., 2024, **9**, 849–860 | **857**
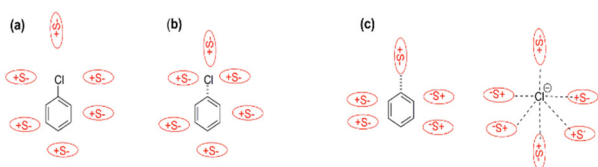
Fig. 8 Stability test of La(1.05)@MOF.

Fig. 9 Effect of solvent on the component: (a) minimal solvation of the reactant molecule, (b) tighter solvation of the transition structure, and (c) separately solvated charged ions.

(such as NO_2) on the *ortho*- or *para*-position react with nucleophiles to afford substitution products.

There are two steps to the reaction mechanism (Fig. 10b): the addition of nucleophile (aniline acts as a strong nucleophile due to NH_2) to form a resonance-stabilized carbanion and a new C–Nu bond in the rate-determining step, followed by elimination of the halogen-leaving group, which exits the group to re-form the aromatic ring.

The EWGs stabilized the intermediate carbanion, and by the Hammond postulate, lowered the energy of the transition state that formed it, thus increasing the number of EWGs, and increasing the reactivity of the aryl halide. Additionally, by increasing the electronegativity of the halogen, the reactivity of the aryl halide has been increased. A more electronegative halogen stabilized the intermediate carbanion by an inductive effect.

Electron-donating groups (EDGs) on the nucleophile aromatic ring (such as OH, OCH_3, and alkyl) accelerate the speed of the reaction because they stabilize the electron-poor carbocation intermediate. This mechanism is accelerated by the presence of metallic catalysts through the empty orbitals, such as d and f, and electron acceptors (stronger Lewis acid) with greater effectiveness also facilitate the reaction.

5. Comparison of photocatalytic efficiencies

A comparative study of the efficiencies of the photocatalysts for the C–N coupling reaction with different types of photocatalysts reported in the literature is significant, and is represented in Table 5.
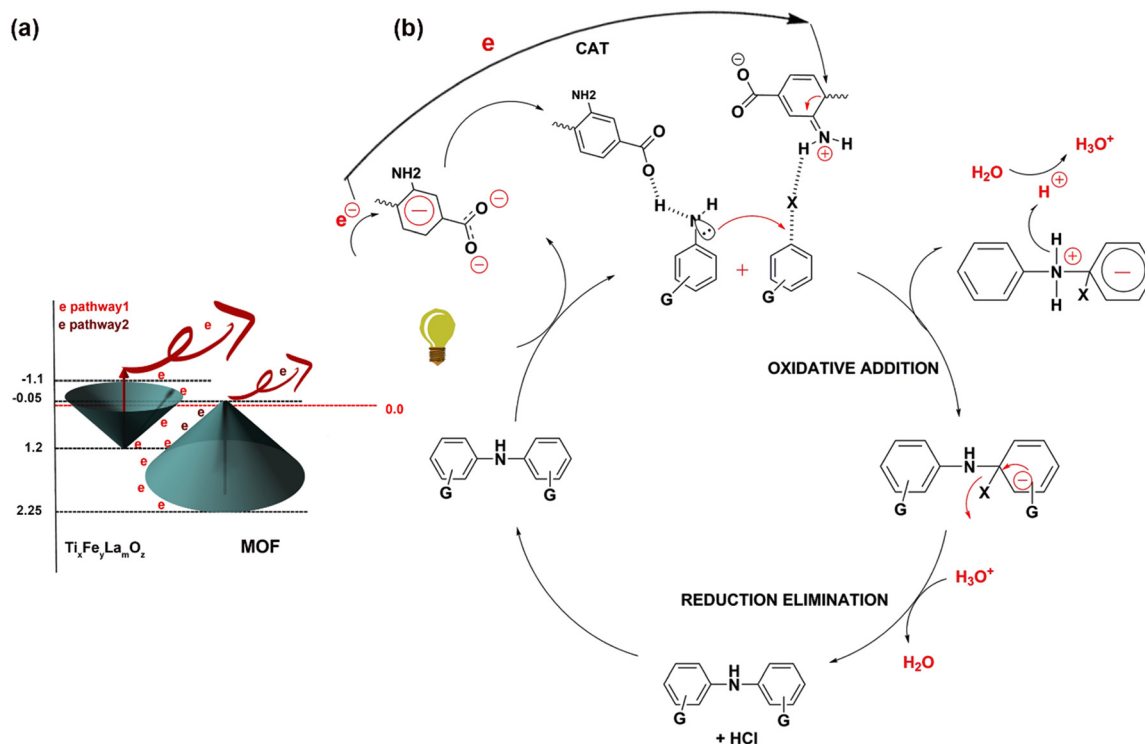

Fig. 10 (a) Pathway of the electron emigration in the photocatalyst. (b) Mechanism of the nucleophilic aromatic substitution.

858 | *React. Chem. Eng.*, 2024, **9**, 849–860

This journal is © The Royal Society of Chemistry 2024

Table 5 Comparative study of the photocatalytic efficiencies of the different photocatalysts

No.	Catalyst	Amount of catalyst	Conversion (%)	Reaction time (h)	Source of light	Temp.©	Ref.
1	Ru(bpy)3@MIL-125	0.1	75	3	VIS	r.t.	42
2	FJI-Y10	2 mmol%	94	6	Xe lamp	40 °C	43
3	MOF-808	10 mg	<1	1	300 W Xe lamp	—	44
4	CdS@Zr-MOFs	10 mg	84	1	300 W Xe lamp	—	44
5	CS@MF-3	10 mg	98	2	Xe lamp	—	44
6	UiO-66-biguanidine/Cu	0.8 mol%	95	4	—	100	45
7	UiO-66-NH2-Mlm/CuO NPs	0.05 g	88	18	—	110	46
8	UiO-66-biguanidine/Cu	0.8 mol%	96	10 h	—	100	47
9	Cu@D-SA	2 mg	93	2 h	—	90	48
10	$Ti_xFe_yLa_mO_z$	0.01 g	91	45	Visible light	r.t.	17

6. Conclusion

In this work, we modified NH_2-MIL-125(Ti) (MOF) with bi-nuclear nanoparticles of $Ti_xFe_yO_z$ and tri-nuclear $Ti_xFe_yLa_mO_z$ nanoparticles. Then, the modified MOFs were applied as photocatalysts for the C–N cross-coupling reaction under visible light. The results showed significant efficiency when MOF was modified by $Ti_xFe_yLa_mO_z$. Thus, the next step was optimizing the obtained composite by loading different concentrations of $Ti_xFe_yLa_mO_z$. Among the different samples, La(1.05)@MOF demonstrated the most optimal photocatalytic behavior to power the C–N coupling reaction under visible light. Although having high surface activity is an important parameter for a photocatalyst, this sample demonstrated the lowest surface activity among the samples.

Additionally, a more robust optical response was achieved by La(1.05)@MOF as compared to the other samples. This proved that the concentration of the loading nanoparticle is crucial for the activity of the final composite, so that electrons can be excited and easily migrate to power the reaction. Aniline and its derivatives were used as an example of a C–N coupling reaction to be powered by La(1.05)@MOF, and the yield of the compound confirmed the ability of this composite to serve as a photocatalyst. In the future, we are going to optimize the same composites to increase the efficiency.

Abbreviations

MOF	NH_2-MIL-125(Ti)
Fe@MOF	$Ti_xFe_yO_z$-NH_2-MIL-125(Ti)
La(1)	$Ti_xFe_yLa_mO_z$ (1)
La(1.05)	$Ti_xFe_yLa_mO_z$ (1.05)
La(1.1)	$Ti_xFe_yLa_mO_z$ (1.1)
La(1.15)	$Ti_xFe_yLa_mO_z$ (1.15)
La(1)@MOF	$Ti_xFe_yLa_mO_z$ (1)-NH_2-MIL-125(Ti)
La(1.05)@MOF	$Ti_xFe_yLa_mO_z$ (1.05)-NH_2-MIL-125(Ti)
La(1.1)@MOF	$Ti_xFe_yLa_mO_z$ (1.1)-NH_2-MIL-125(Ti)
La(1.15)@MOF	$Ti_xFe_yLa_mO_z$ (1.15)-NH_2-MIL-125(Ti)

Conflicts of interest

The authors declare no competing financial interests.

References

1 M. C. Deem, J. S. Derasp, T. C. Malig, K. Legard, C. P. Berlinguette and J. E. Hein, *Nat. Commun.*, 2022, **13**, 2869.

2 S. L. Goldschmid, N. E. Soon Tay, C. L. Joe, B. C. Lainhart, T. C. Sherwood, E. M. Simmons, M. Sezen-Edmonds and T. Rovis, *J. Am. Chem. Soc.*, 2022, **144**, 22409–22415.

3 R. Anbarasan, A. Thamizhlarasan, Y.-C. Liu and K.-L. Tung, *J. Taiwan Inst. Chem. Eng.*, 2023, **142**, 104613.

4 C. M. Simon, S. L. Dudra, R. T. McGuire, M. J. Ferguson, E. R. Johnson and M. Stradiotto, *ACS Catal.*, 2022, **12**, 1475–1480.

5 S. Rasaily, D. Sharma, S. Pradhan, N. Diyali, S. Chettri, B. Gurung, S. Tamang and A. Pariyar, *Inorg. Chem.*, 2022, **61**, 13685–13699.

6 T. You and J. Li, *Org. Lett.*, 2022, **24**, 6642–6646.

7 P. Lei, Y. Wang, C. Zhang, Y. Hu, J. Feng, Z. Ma, X. Liu, R. Szostak and M. Szostak, *Org. Lett.*, 2022, **24**, 6310–6315.

8 J. Zhan, L. Zhu, W. Ren, B. Wang, X. Zhao, X. Zhang, X. Zhang and Y. Xie, *Adv. Synth. Catal.*, 2023, **365**, 1678–1684.

9 J. Zhang, P. Zhang, Y. Ma and M. Szostak, *Org. Lett.*, 2022, **24**, 2338–2343.

10 M. V. Mane, S. Dutta, L. Cavallo and B. Maity, *ACS Catal.*, 2023, **13**, 6249–6260.

11 M. Sharma, M. K. Mandal, S. Pandey, R. Kumar and K. K. Dubey, *ACS Omega*, 2022, 7, 33572–33586.

12 K. Al-hamoud, M. R. Shaik, M. Khan, H. Z. Alkhathlan, S. F. Adil, M. Kuniyil, M. E. Assal, A. Al-Warthan, M. R. H. Siddiqui, M. N. Tahir, S. T. Khan, A. A. Mousa and M. Khan, *ACS Omega*, 2022, 7, 4812–4820.

13 B. Palajonnala Narasaiah, P. Banoth, A. G. Bustamante Dominguez, B. K. Mandal, C. K. Kumar, C. H. W. Barnes, L. De Los Santos Valladares and P. Kollu, *ACS Omega*, 2022, 7, 26174–26189.

14 Y. N. Rajeev, C. M. Magdalane, G. Ramalingam, L. B. Kumar, N. Alwadai and M. S. Al-Buriahi, *Appl. Phys. A: Mater. Sci. Process.*, 2022, **128**, 299.

This journal is © The Royal Society of Chemistry 2024

React. Chem. Eng., 2024, **9**, 849–860 | **859**

15 M. A. Ávila-López, T. E. Lara-Ceniceros, F. E. Longoria, A. A. Elguezabal, A. Martínez de la Cruz, M. A. Garza-Navarro and J. Bonilla-Cruz, *ACS Appl. Nano Mater.*, 2022, **5**, 11437–11446.

16 H. Yu, H. Irie, Y. Shimodaira, Y. Hosogi, Y. Kuroda, M. Miyauchi and K. Hashimoto, *J. Phys. Chem. C*, 2010, **114**, 16481–16487.

17 M. Rafsanjani Dehghazi, Y. Absalan, M. Gholizadeh, M. Razavi and K. Souri, *ACS Appl. Nano Mater.*, 2023, **6**, 1106–1118.

18 Y. Li, H. Zhang, Z. Guo, J. Han, X. Zhao, Q. Zhao and S.-J. Kim, *Langmuir*, 2008, **24**, 8351–8357.

19 S. Klosek and D. Raftery, *J. Phys. Chem. B*, 2001, **105**, 2815–2819.

20 A. Ozawa, M. Yamamoto, T. Tanabe and T. Yoshida, *ACS Omega*, 2019, **4**, 20424–20429.

21 H. B. Ahmad, N. Saad and H. E. Emam, *Surf. Interfaces*, 2021, **25**, 101175.

22 Bharti, J. S. Jangwan, V. Kumar, S. S. Kumar, A. Kumar and P. Yadav, *ACS Symp. Ser.*, 2021, 125–154.

23 A. Kumar, S. Kumar, S. Duhan, A. Kumar, S. Devi and P. Kumar, *ACS Symp. Ser.*, 2021, 247–255.

24 B. Uttam and R. Kumar, *ACS Symp. Ser.*, 2021, 125–154.

25 D.-F. Lu, Y.-P. Han, Y. Sun, F. Wang and J. Zhang, *Cryst. Growth Des.*, 2023, **23**, 3778–3784.

26 L. Öhrström and F. M. Amombo Noa, *Metal-Organic Frameworks*, American Chemical Society, Washington, DC, USA, 2021.

27 Z. Liu, B. Xiong, Y. Dong, Y. Ning and D. Li, *Inorg. Chem.*, 2022, **61**, 16203–16210.

28 D. Ryu and J. Kim, *J. Phys. Chem. C*, 2023, **127**, 10384–10390.

29 M. Samaniyan, M. Mirzaei, R. Khajavian, H. Eshtiagh-Hosseini and C. Streb, *ACS Catal.*, 2019, **9**, 10174–10191.

30 M. Vázquez-González and I. Willner, *Langmuir*, 2018, **34**, 14692–14710.

31 X. Zeng, Z. Wu, T. Nie, C. Zhao, R. Yu, G. D. Stucky and Y. Gao, *ACS Appl. Nano Mater.*, 2022, **5**, 11474–11483.

32 A. V. Desai, S. M. Vornholt, L. L. Major, R. Ettlinger, C. Jansen, D. N. Rainer, R. de Rome, V. So, P. S. Wheatley, A. K. Edward, C. G. Elliott, A. Pramanik, A. Karmakar, A. R. Armstrong, C. Janiak, T. K. Smith and R. E. Morris, *ACS Appl. Mater. Interfaces*, 2023, **15**, 9058–9065.

33 F. E. Salvador, J. O. Barajas and W.-Y. Gao, *Inorg. Chem.*, 2023, **62**, 3333–3337.

34 H. Zhang, Y. Lv, T. Tan and D. van der Spoel, *J. Phys. Chem. B*, 2016, **120**, 477–484.

35 Y. Shu, Q. Ye, T. Dai, Q. Xu and X. Hu, *ACS Sens.*, 2021, **6**, 641–658.

36 Z. Cui, Q. Liu, J. Zhu, H. Wang, M. Gao, W. Wang, M. F. Yuen, J. Hu, H. Chen and R. Zou, *Nano Lett.*, 2023, **23**, 1600–1607.

37 H. E. Emam, H. B. Ahmed, E. Gomaa, M. H. Helal and R. M. Abdelhameed, *J. Photochem. Photobiol., A*, 2019, **383**, 111986.

38 C. E. Housecroft and E. C. Constable, *J. Mater. Chem. C*, 2022, **10**(12), 4456–4482.

39 S. Liu, J. Dong, X. Fang, X. Yan, H. Zhang, Y. Hu, Q. Zhu, R. Li, Q. Liu, S. Liu, C. Liao and G. Jiang, *Environ. Sci. Technol.*, 2023, **57**, 5380–5390.

40 H. E. Emam, M. El-Shahat and R. M. Abdelhameed, *J. Hazard. Mater.*, 2021, **414**, 125509.

41 H. E. Emam, H. B. Ahmed, E. Gomaa, M. H. Helal and R. M. Abdelhameed, *Carbohydr. Polym.*, 2021, **226**, 118163.

42 X. Yang, T. Huang, S. Gao and R. Cao, *J. Catal.*, 2019, **378**, 248–255.

43 F.-J. Zhao, G. Zhang, Z. Ju, Y.-X. Tan and D. Yuan, *Inorg. Chem.*, 2020, **59**, 3297–3303.

44 K. Gao, H. Li, Q. Meng, J. Wu and H. Hou, *ACS Appl. Mater. Interfaces*, 2021, **13**, 2779–2787.

45 N. R. Jogdand, B. B. Shingate and M. S. Shingare, *Tetrahedron Lett.*, 2009, **50**, 4019–4021.

46 S. Najari, M. Jafarzadeh and K. Bahrami, *J. Heterocycl. Chem.*, 2019, **56**, 2853–2865.

47 H. Veisi, N. Neyestani, M. Pirhayati, S. Ahany Kamangar, S. Lotfi, T. Tamoradi and B. Karmakar, *RSC Adv.*, 2021, **11**, 22278–22286.

48 T. Maity, P. Ghosh, S. Das, D. Saha and S. Koner, *New J. Chem.*, 2021, **45**, 5568–5575.